

Inferences from GRB 190114C: Magnetic Field and Afterglow of BdHN

JORGE A. RUEDA,^{1,2,3,4} REMO RUFFINI,^{1,2,3,5,6} MILE KARLICA,^{1,2,5} RAHIM MORADI,^{1,2,7} AND YU WANG^{1,2,7}¹*ICRA, Dipartimento di Fisica, Sapienza Università di Roma, P.le Aldo Moro 5, 00185 Rome, Italy.*²*ICRANet, P.zza della Repubblica 10, 65122 Pescara, Italy. yu.wang@icranet.org*³*ICRANet-Rio, Centro Brasileiro de Pesquisas Físicas, Rua Dr. Xavier Sigaud 150, 22290-180 Rio de Janeiro, Brazil.*⁴*INAF, Istituto di Astrofisica e Planetologia Spaziali, Via Fosso del Cavaliere 100, 00133 Rome, Italy.*⁵*Université de Nice Sophia Antipolis, CEDEX 2, Grand Château Parc Valrose, Nice, France.*⁶*INAF, Viale del Parco Mellini 84, 00136 Rome, Italy.*⁷*INAF – Osservatorio Astronomico d'Abruzzo, Via M. Maggini snc, I-64100, Teramo, Italy.*

(Dated: December 15, 2024)

ABSTRACT

GRB 190114C is the first binary-driven hypernova (BdHN) fully observed from the initial supernova (SN) shockwave breakout to the eventual emergence of the optical SN signal. It offers an unprecedented support for the BdHN theory. BdHNe comprise four subclasses of long gamma-ray bursts (GRBs) with progenitors as a binary system composed of a carbon-oxygen star (CO_{core}) and a neutron star (NS) or a black hole (BH) companion. The CO_{core} explodes as a supernova (SN) leaving at its center a new NS (ν NS). The SN hypercritically ejecta accretes onto the NS/BH companion. BdHNe I are the tightest binaries where the accretion leads the initial NS gravitationally collapses to a BH. In BdHN II the accretion onto the NS is lower, there is no BH formation. We infer for GRB 190114C and other selected examples of BdHN I (GRB 130427A, GRB 160509A, GRB 160625B), BdHN II (GRB 180728A) the intensity and structure of the ν NS magnetic field needed for the explanation of the afterglow via synchrotron emission powered by the newborn NS. In the case of the BdHNe I, we infer as well the properties of the magnetic field around the newborn BH, requested for the explanation of the observed GeV emission through what we have called the *inner engine*: the rotating BH surrounded by a magnetic field and matter from the SN ejecta. We also discuss the possible nature of the magnetic field both the one of the ν NS and the one around the newborn BH.

Keywords: gamma-ray bursts: general — binaries: general — stars: neutron — supernovae: general — black hole physics

1. INTRODUCTION

The binary driven hypernova (BdHN) model has been introduced for the explanation of long-duration gamma-ray bursts (GRBs) and it follows the induced gravitational collapse (IGC) paradigm (Rueda & Ruffini 2012; Fryer et al. 2014). The progenitor system is a binary system composed of a carbon-oxygen core (CO_{core}) and a magnetized ($B \sim 10^{13}$ G) neutron star (NS) companion in tight orbit (period of the order of few minutes). At the end of its thermonuclear evolution, the core-collapse of the CO_{core} leads to a type Ib/c supernova (SN) which, owing to the short orbital period, produces a hypercritical (i.e. highly super-Eddington) accretion process onto the NS companion. The material hits the NS surface developing and outward shock which creates an accretion “atmosphere” of very high density and temperature on

top the NS. These conditions turn to be appropriate for the thermal production of positron-electron (e^+e^-) pairs which, when annihilating, leads to a copious production of neutrino-antineutrino ($\nu\bar{\nu}$) which turn to be the most important carriers of the gravitational energy gain of the accreting matter, allowing the rapid and massive accretion to continue. We refer to Fryer et al. (2014); Becerra et al. (2016, 2018) for additional details on the processes of hypercritical accretion and on the ν -physics at work.

Depending on the specific system parameters (mass of the binary components, orbital period, SN explosion energy, etc; Becerra et al. 2016, 2019), two possible fates for the NS are possible (Becerra et al. 2015, 2016, 2018). For short binary periods, i.e. ~ 5 min, the NS reaches the critical mass for gravitational collapse and forms a BH (see e.g. Fryer et al. 2015; Becerra et al. 2015, 2016,

2019). We have called this kind of system a BdHN type I (Wang et al. 2019b). A BdHN emits an isotropic energy $E_{\text{iso}} \gtrsim 10^{52}$ erg and gives origin to a new binary composed by the ν NS formed by the SN and the BH formed by the collapse of the NS. For longer binary periods, the hypercritical accretion onto the NS is not sufficient to bring it to the critical mass and a more massive NS (MNS) is formed. We have divided this kind of system in BdHN of type II, for 10^{50} erg $\lesssim E_{\text{iso}} \lesssim 10^{52}$ erg, and BdHN of type III for $E_{\text{iso}} \lesssim 10^{50}$ erg (Wang et al. 2019b). A BdHN II/III gives origin to a new binary composed by the ν NS and the MNS.

The BdHNe I represent, as we know today, the totality of long GRBs with energy larger than 10^{52} erg while, the BdHN II and III with their energy less than 10^{52} erg, are far from unique and there is a variety of long GRBs in addition to them which might have similar energetics; e.g. double white dwarf (WD-WD) mergers and NS-WD mergers (see Ruffini et al. 2016, 2018d; Wang et al. 2019b, for details).

Three-dimensional, numerical smoothed-particle-hydrodynamics (SPH) simulations of BdHNe have been recently presented in Becerra et al. (2019). These simulations improve and extends the previous ones by Becerra et al. (2016). A fundamental contribution of these simulations has been to provide a visualisation of the morphology of the SN ejecta which is modified from the initial spherical symmetry. A low-density cavity is carved by the NS companion and then, once it collapses, by the BH formation process (see also Ruffini et al. 2019c). Such an asymmetric density distribution leads to a dependence of the GRB description as a function of the observer viewing angle: in the orbital/equatorial plane or in the plane orthogonal to it (Becerra et al. 2016; Ruffini et al. 2018b,e; Becerra et al. 2019) and as a function of the orbital period of the binary, in the simulation of Fig. 1 about 300 s (Ruffini et al. 2018e).

In the case of BdHNe I, i.e. when a BH is formed, the BH rotation in presence of a surrounding magnetic field (possibly inherited from the NS; see Sec. 4) and matter from the SN ejecta, conform what we have called the *inner engine* of the high-energy emission of long GRBs (see Ruffini et al. 2018f,c, 2019c,a, for details). The electromagnetic field of the *inner engine* is mathematically described by the Wald’s solution (Wald 1974). The BdHNe parameters imply that the induced electric field around the BH is initially overcritical, then able to create an electron-positron (e^+e^-) pair plasma via vacuum polarization. The e^+e^- plasma self-accelerates to ultra-relativistic velocities reaching transparency at the right time and energies to explain the GRB prompt emission

in the gamma-rays. The electric field, along the BH rotation axis, is able to accelerate protons up to 10^{21} eV, leading to ultra high-energy cosmic rays (UHECRs). In the off-polar directions protons are subjected to energy losses via synchrotron radiation which explains the GeV emission (Ruffini et al. 2018f,c).

The SN transforms into a hypernova (HN) as a result of the energy and momentum transfer of the e^+e^- plasma (Ruffini et al. 2018e; Becerra et al. 2019). The SN shock breakout and the hypercritical accretion can be observed as X-ray precursors (Becerra et al. 2016; Wang et al. 2019b). The e^+e^- feedback also produces gamma- and X-ray flares observed in the early afterglow (Ruffini et al. 2018b). There is then the most interesting emission episode which is related to the ν NS originated from the SN explosion. Namely, the synchrotron emission by relativistic electrons, injected from the ν NS pulsar emission into the HN ejecta in presence of the ν NS magnetic field, explain the X-ray afterglow and its power-law luminosity (Ruffini et al. 2018a; Wang et al. 2019b). Finally, the HN is observed in the optical bands few days after the GRB trigger, powered by the energy release of the nickel decay.

A scheme that summarizes all the above physical and observational features of a BdHN I is shown in Fig. 2.

As we have seen, the magnetic field, the one of the ν NS as well as the one surrounding the newborn BH, are crucial properties in a BdHN and for the explanation of the prompt emission, the GeV emission, and the afterglow. We focus in this work on the determination of the magnetic field properties and discuss as well the possible nature of the fields. For this we analyze specific examples of BdHNe I and II. For BdHNe I we study the recent GRB 190114C with its exquisite observational data (Ruffini et al. 2019c,a), GRB 130427A (Ruffini et al. 2018a; Wang et al. 2019b), GRB 160509A and GRB 160625B. As an example of BdHN II, GRB 180728A (Wang et al. 2019b).

The article is organized as follows. In Sec. 2 we recall the observational properties of these GRBs. We study in Sec. 3 we infer the magnetic field of the ν NS based on the framework presented in Wang et al. (2019b) for the explanation of the X-ray afterglow, which we here recall and apply to the present sources. This treatment follows the well tested cases of two representative examples: GRB 130427A as an archetype of BdHN I and GRB 180827A as an archetype of BdHN II. The nature of the found magnetic field is discussed in Sec. 4. The inferences on the magnetic field embedding the newborn BH are presented in Sec. 5. We use our recent works for the explanation of the high-energy GeV emission observed in BdHNe I (Ruffini et al. 2018f,c, 2019c), based

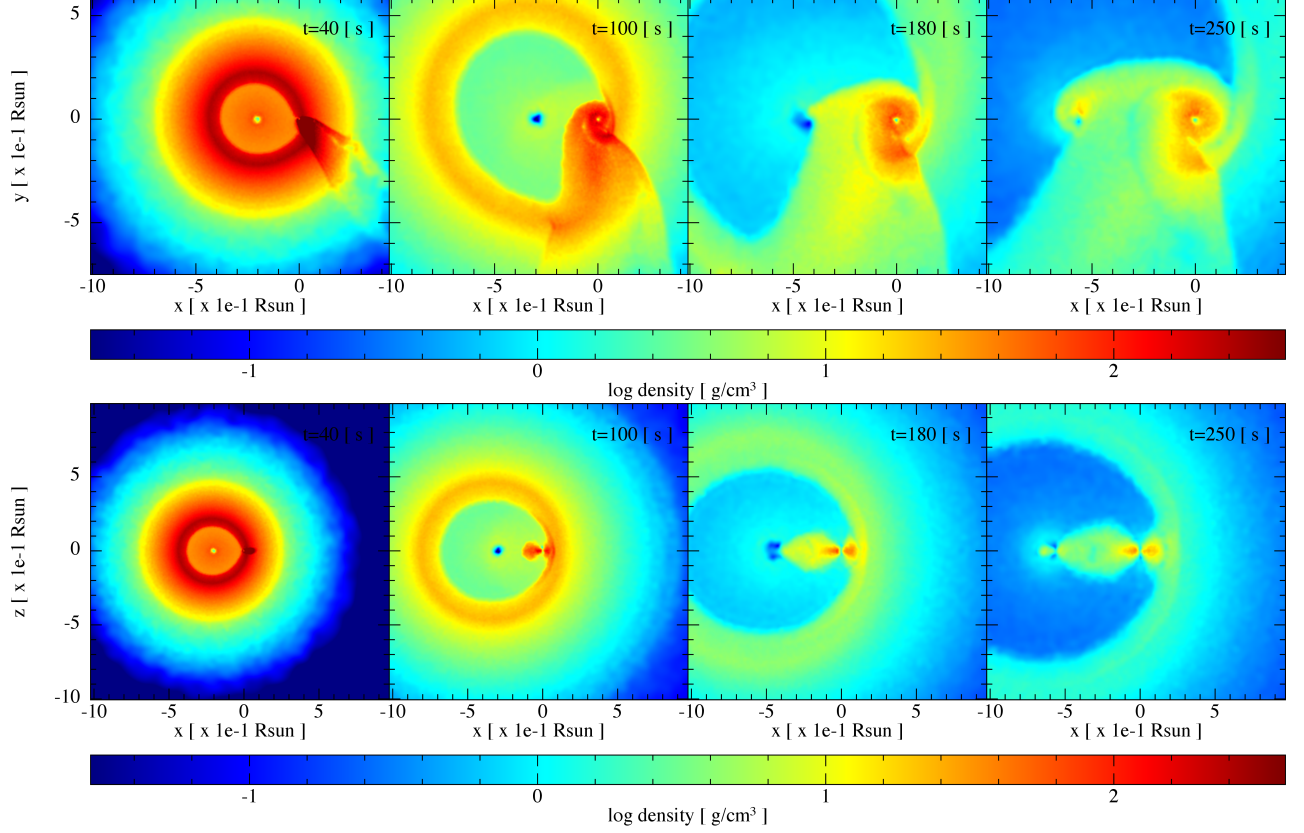


Figure 1. SPH simulation of a BdHN I; Model ‘25M1p1e’ of Table 2 in [Becerra et al. \(2019\)](#). The binary progenitor is composed of a CO_{core} of $\approx 7 M_{\odot}$ produced by a zero-age main-sequence star (ZAMS) star of $25 M_{\odot}$ (see Table 1 in [Becerra et al. 2019](#)), and a $2 M_{\odot}$ NS companion. The orbital period is ≈ 5 min. Each frame, from left to right, corresponds to selected increasing times being $t = 0$ s the instant of the SN shock breakout. The upper panel shows the mass density on the equatorial plane and the lower panel the plane orthogonal to the equatorial one. The reference system is rotated and translated to align the x-axis with the line joining the binary components. The origin of the reference system is located at the NS companion position. The first frame corresponds to $t = 40$ s and it shows that the particles entered into the NS capture region forms a tail behind it. These particles then circularize around the NS forming a thick disk which is already visible in the second frame at $t = 100$ s. Part of the SN ejecta is also attracted by the νNS accreting onto it; this is appreciable in the third frame at $t = 180$ s. At $t = 250$ s (about one orbital period), a disk structure has been formed around the νNS and the NS companion. To guide the eye, the νNS is at the x-coordinate: -2.02 , -2.92 , -3.73 and -5.64 for $t = 40$ s, 100 s, 180 s and 250 s, respectively. This figure has been produced with the *SNsplash* visualization program ([Price 2011](#)). The figure has been taken from [Becerra et al. \(2019\)](#) with the permission of the authors.

on the aforementioned *inner engine*. In Sec. 6 we discuss the possible nature of this magnetic field. Finally, in Sec. 7 we outline our conclusions.

2. GRBS (BDHNE I) OF THE PRESENT WORK

GRB 130427A is one of the best observed GRBs, it locates at redshift $z \sim 0.34$ ([Levan et al. 2013](#)), more than 50 observatories participated the observation. It hits the record of the brightness in the gamma-ray emission, so that Fermi-GBM was saturated. It also hits the record of GeV observation with more than 500 photons above 100 MeV received, and the GeV emission observed till $\sim 10^4$ s ([Ackermann et al. 2014](#)).

The shape of its prompt emission consists a ~ 3 s precursor, followed by a multi peaked pulse lasting ~ 10 s.

At time ~ 120 s, an additional flare appears, then it enters the afterglow ([Maselli et al. 2014](#)). The X-ray afterglow is observed by Swift and NuStar. Swift covers discretely from ~ 150 s to $\sim 10^7$ s, and NuStar observes three epochs, starting approximately 1.2, 4.8 and 5.4 days, for observational duration 30.5, 21.2, and 12.3 ks ([Kouveliotou et al. 2013](#)). The power-law decay index of the late time afterglow after ~ 2000 s gives ~ -1.32 ([Ruffini et al. 2015](#)).

The optical spectrum reveals that 16.7 days after the GRB trigger, a typical of SNe Ic emerges ([Xu et al. 2013](#); [Li et al. 2018](#)), as predicted by [Ruffini et al. \(2013\)](#).

GRB 160509A, at redshift $z \sim 1.17$ ([Tanvir et al. 2016](#)), is a strong source of GeV emission, including a

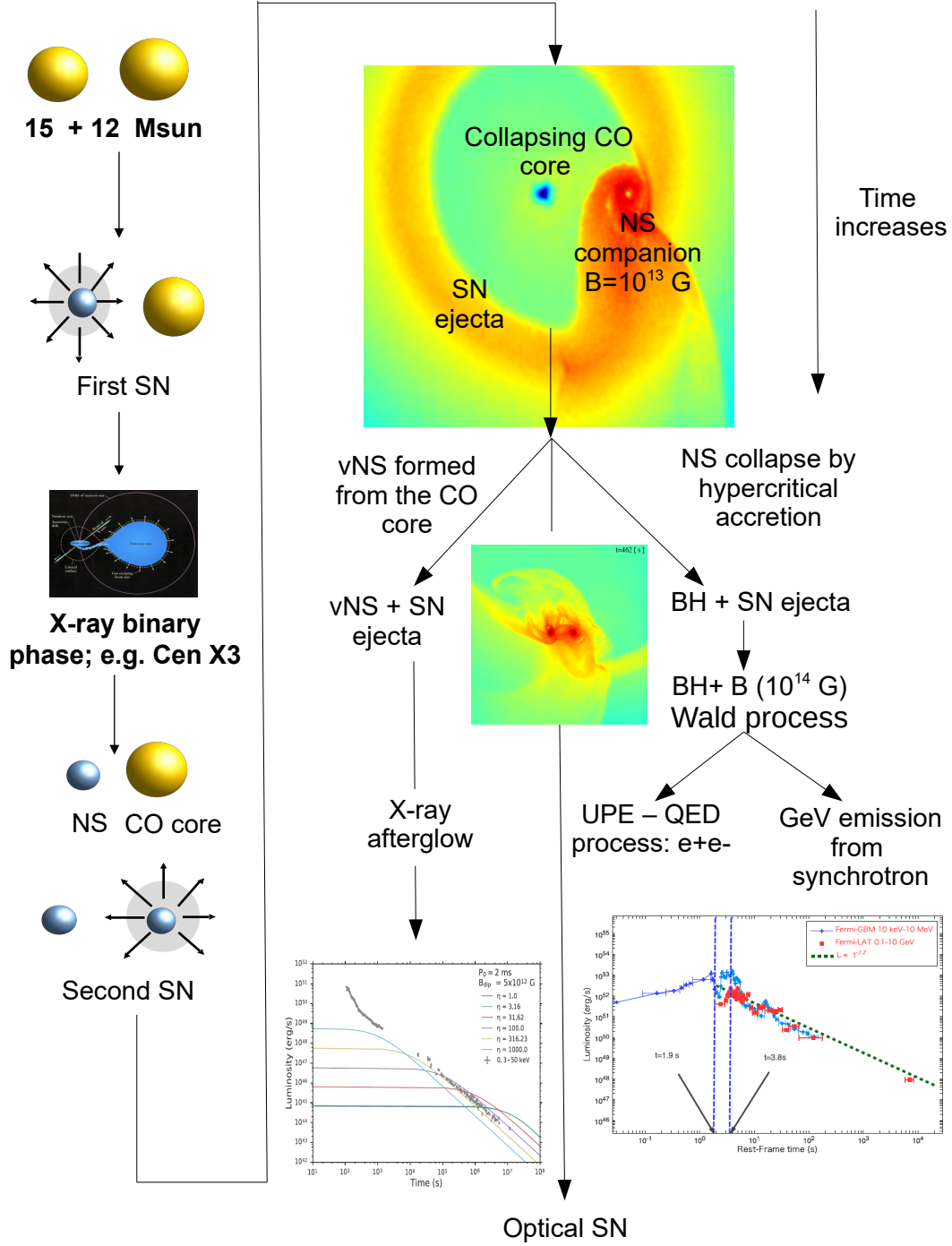


Figure 2. Schematic example of the evolutionary path of a massive binary all the way up to the formation of a BdHN I. The BdHN progenitor is a binary composed of a CO_{core} and a magnetized ($B \sim 10^{13}$ G) NS companion in a very compact orbit (period of the order of minutes). To reach the BdHN stage the binary has to survive two SN events: the first SN forms the NS and the second one the ν NS (core-collapse of the CO_{core}). The SN ejecta produce a massive and rapid accretion process onto the NS companion leading to its gravitational collapse forming a BH. Conservation of magnetic flux and possibly additional MHD processes amplify the magnetic field from the NS value to $B \sim 10^{14}$ G around the BH. While the SN matter expands, before escaping from the system it surrounds both the ν NS and the BH. The B -field together with the BH rotation triggers the “Wald” process which induces an electric field. This E -field explains both the UPE in the gamma-rays through the transparency of the self-accelerating e^-e^+ pair plasma created by the QED process of vacuum breakdown, and the GeV emission through synchrotron emission of accelerated protons in the B -field. The interaction of the ν NS pulsar emission with the SN ejecta explains the X-ray afterglow. Finally, after about 15 days, the optical emission of the SN produced by the energy release of the decay of Nickel, is observed.

52 GeV photon arriving at 77 s, and a 29 GeV photon arriving ~ 70 ks (Laskar et al. 2016).

GRB 160509A consists of two emission periods, 0–40 s and 280 – 420s (Tam et al. 2017). The first period exhibits a single pulse structure for sub-MeV emission, and a double pulses structure for ~ 100 MeV emission. The second period is in the sub-MeV energy range with double pulses structure. Swift-XRT started the observation ~ 7000 s after the burst, with a shallow power-law decay of index ~ -0.6 , followed by a normal decay of power-law index ~ -1.45 after 5×10^4 s (Tam et al. 2017).

There is no supernova association reported, the optical signal of supernova can hardly be confirmed for GRBs with redshift > 1 , since the absorption is intense (Woosley & Bloom 2006).

GRB 160625B, at redshift 1.406 (Xu et al. 2016), is a bright GRB with the speciality that the polarisation has been detected. Fermi-LAT has detected more than 300 photons with energy > 100 MeV (Lü et al. 2017).

The gamma-ray light curve has three distinct pulses (Li 2018; Zhang et al. 2018). The first short pulse is totally thermal, it lasts ~ 2 s; the second bright pulse starts from ~ 180 s and ends at ~ 240 s; the last weak pulse emerges from ~ 330 s and lasts ~ 300 s. The total isotropic energy reaches $\sim 3 \times 10^{54}$ erg (Alexander et al. 2017; Lü et al. 2017).

Swift-XRT starts the observation at late time ($> 10^4$ s), a power-law behaviour with decaying index ~ -1.25 .

There is no supernova confirmation, possibly it is due to the redshift > 1 (Woosley & Bloom 2006).

GRB 190114C, at redshift $z \sim 0.42$ (Selsing et al. 2019), is the first GRB with TeV photon detection by MAGIC (Mirzoyan et al. 2019). It has twin features as GRB 130427A (Wang et al. 2019a), and it caught great attention as well.

The prompt emission of GRB 190114C starts by a multi-peaked pulse, its initial ~ 1.5 s is non-thermal, then followed by a possible thermal emission till ~ 1.8 s. The confident thermal emission exists during the peak of the pulse, from 2.7 – 5.5 s. The GeV emission starts from 2.7 s, initiated with a spiky structure, then follows a power-law decay with index ~ -1.2 (Ruffini et al. 2019c). The GeV emission is very luminous, more than 200 s photons with energy > 100 MeV are received. The X-ray afterglow observed by Swift-XRT shows a persistent power-law decay behaviour, with decaying index ~ 1.35 (Wang et al. 2019a).

An continuous observational campaign lasting ~ 50 days unveiled the supernova emergence at ~ 15 days

after the GRB (Melandri et al. 2019), which is consistent with the prediction of 18.8 ± 3.7 days after the GRB by Ruffini et al. (2019b).

3. MAGNETIC FIELD OF THE ν NS AND THE X-RAY AFTERGLOW OF GRB 190114C

3.1. Synchrotron Emission

As a consequence of interaction between the ν NS and the magnetized HN ejecta we expect copious amounts of relativistic electrons radiating away energy within optically thin region through synchrotron radiation mechanism. The origin of this accelerated electrons can be found in an interplay between particle acceleration mechanisms happening in ν NS pulsar surroundings and the one taking place in HN ejecta (Ruffini et al. 2018a). To fully follow the temporal behaviour of radiation spectra it is necessary to solve the kinetic equation for the electron distribution within HN, which in the case of homogeneous and isotropic emitter is given with

$$\frac{\partial N(\gamma, t)}{\partial t} = \frac{\partial}{\partial \gamma}(b(\gamma, t)N(\gamma, t)) - \frac{N(\gamma, t)}{\tau} + Q(\gamma, t), \quad (1)$$

where $N(\gamma, t)$ is the electron number distribution as a function of electron's energy $\gamma = E/m_e c^2$, $b(\gamma, t)$ are the electron energy losses, $Q(\gamma, t)$ is the injection spectra of electrons and τ is the characteristic escape time which for all practical purposes concerning GRB afterglow phase can be taken as infinite value $\tau \rightarrow \infty$. Electron injection spectra is determined through the particle acceleration processes involved and can be generally described by

$$Q(\gamma, t) = Q_0(t)\gamma^{-p}\theta(\gamma_{\max} - \gamma)\theta(\gamma - \gamma_{\min}) \quad (2)$$

with p the injection spectra power-law index, $Q_0(t)$ the time dependent part of particle injection, γ_{\min} and γ_{\max} being minimum and maximum energy of injected/accelerated electrons in the emitting region. The injected electron spectra given by equation 2 comes from the energy budget of the ejecta and its efficiency to convert energy from kinetic energy of bulk motion into the non-thermal energy of accelerated particles leading to injection power given by

$$L(t) = Q_0(t)m_e c^2 \int_{\gamma_{\min}}^{\gamma_{\max}} \gamma^{-p+1} d\gamma, \quad (3)$$

which following the well established knowledge of time power law behaviour of both HN and pulsar wind nebula phenomena can be simply described by a following formula

$$L(t) = L_0 \left(1 + \frac{t}{\tau_0}\right)^{-k}, \quad (4)$$

where L_0 , k and τ_0 are assessed by fitting of the observed afterglow light curve. On the other hand it is worth noticing that in HN magnetized by ν NS dominant and most important energy losses will be adiabatic energy losses and synchrotron energy losses

$$b(\gamma, t) = \frac{\dot{R}(t)}{R(t)}\gamma + \frac{4}{3} \frac{\sigma_T}{m_e c} \frac{B(t)^2}{8\pi} \gamma^2, \quad (5)$$

where $R(t)$ is the size of emitter easily computed if we know the expansion velocity $\dot{R}(t)$, σ_T is the Thomson cross section and $B(t)$ is the magnetic field strength expected to have toroidal configuration given by

$$B(t) = B_0 \frac{R(t_0)}{R(t)}, \quad (6)$$

since $R(t)$ is much larger than light cylinder radius $R_{LC} = cP/2\pi$ of the ν NS. The time t_0 is adopted as equal to the timescale τ_0 . Since most of the crucial inputs within equation 1 are time dependent, to solve it we developed a code using the tridiagonal matrix solver routine given in Press et al. (1992). Consequent time dependent solution $N(\gamma, t)$ was utilized to compute the synchrotron luminosity L_{syn} using the single electron synchrotron spectra $P_{\text{syn}}(\nu, \gamma, B(t))$ presented in Aharonian et al. (2010)

$$L_{\text{syn}}(\nu, t) = \int_1^{\gamma_{\text{max}}} N(\gamma, t) P_{\text{syn}}(\nu, \gamma, B(t)) d\gamma. \quad (7)$$

The exquisite quality of data ranging from radio to γ -ray bands present in case of GRB 130427A clearly presented itself as a prototype candidate. Alongside the multiwavelength observations of aforementioned GRB, it presented us with rare information of expansion velocities, both from early stages around 10^2 seconds with rather mildly relativistic expansion velocity of $0.8c$ (obtained from the expansion of present thermal component) and from later stages of afterglow around 10^6 seconds decelerating to rather non-relativistic velocity of $0.1c$ (obtained through observations of Fe II emission lines).

To describe the expansion velocity of GRB 130427A we therefore adopted a rather conservative ballistic expression given by

$$\dot{R}(t) = \begin{cases} v_0 - a_0 t & t \leq 10^6 \text{ s} \\ v_f & t > 10^6 \text{ s} \end{cases}, \quad (8a)$$

$$R(t) = \begin{cases} v_0 t - a_0 t^2/2 & t \leq 10^6 \text{ s} \\ 1.05 \times 10^{16} \text{ cm} + v_f t & t > 10^6 \text{ s} \end{cases}. \quad (8b)$$

c—c

Table 1. Parameters used for simulation of GRB 130427A.

Parameter	Value
B_0	$5.0 \times 10^5 \text{ G}$
R_0	$2.4 \times 10^{12} \text{ cm}$
L_0	$2.0 \times 10^{51} \text{ erg/s}$
k	1.58
τ_0	$1.0 \times 10^2 \text{ s}$
p	1.5
γ_{min}	4.0×10^3
γ_{max}	5.0×10^5

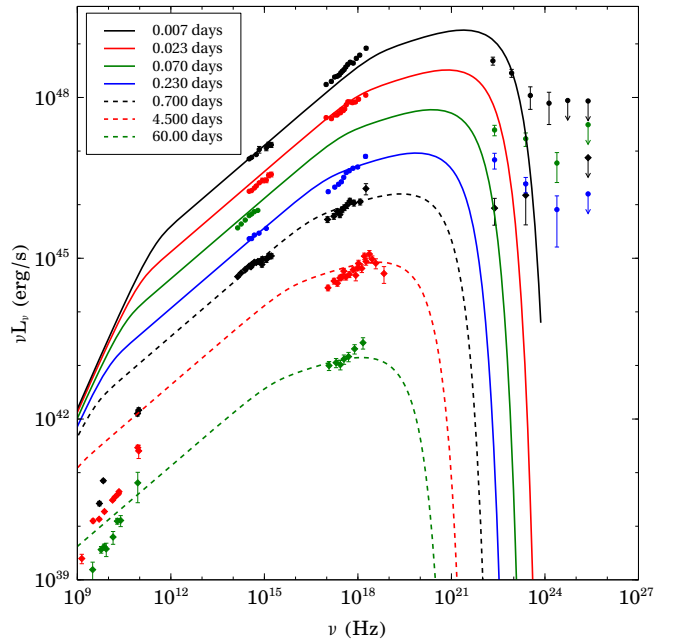


Figure 3. Model evolution of synchrotron spectral luminosity at various times compared with measurements in various spectral bands for GRB 130427A.

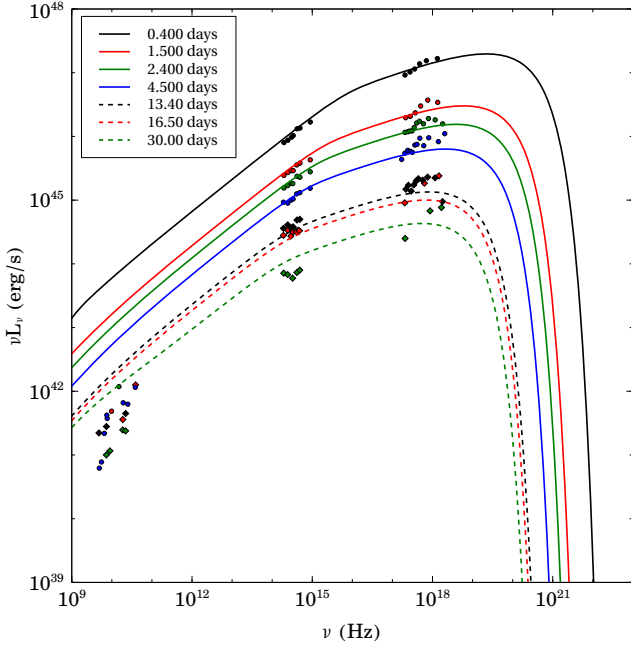
with $v_0 = 2.4 \times 10^{10} \text{ cm s}^{-1}$, $a_0 = 2.1 \times 10^4 \text{ cm s}^{-2}$ and $v_f = 3 \times 10^9 \text{ cm s}^{-1}$.

The parameters necessary to fit the time resolved spectral data are given in Table 1 leading to a rather well fitting shown on figure 3.

As shown on figure 5 we that our model fits very well the X-ray light curve, while it is not capable to fit the GeV data. This difference comes from the fact that within BdHN paradigm we expect the GeV photons to mostly come from activity connected with the newly formed black hole (BH) which is not included in this model. On the other hand radio data show lack of expected flux which comes from synchrotron self absorption processes which are rather complicated to model in

Table 2. Parameters used for simulation of GRB 160625B.

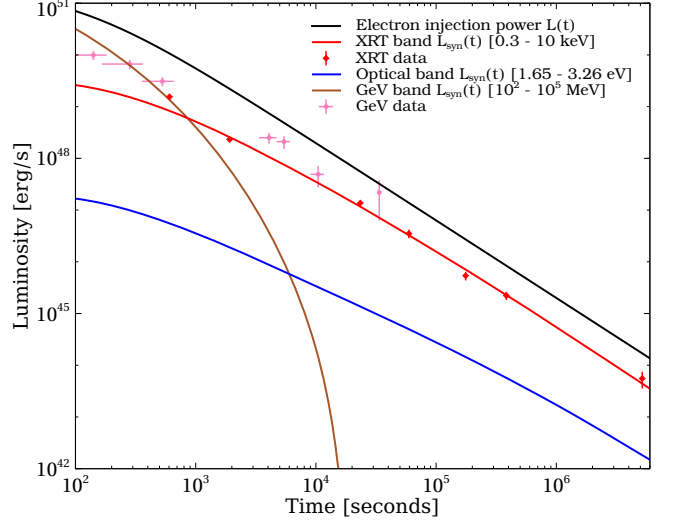
Parameter	Value
B_0	1.0×10^6 G
R_0	1.2×10^{11} cm
L_0	8.44×10^{52} erg/s
k	1.42
τ_0	5.0×10^0 s
p	1.5
γ_{\min}	4.0×10^3
γ_{\max}	1.0×10^6

**Figure 4.** Model evolution of synchrotron spectral luminosity at various times compared with measurements in various spectral bands for GRB 160625B.

current numerical framework but can be thoroughly neglected at frequencies above 10^{14} Hz.

Even with the limitations mentioned this fitting of GRB 130427A shows an important challenge to the traditional treatment of GRB afterglow questioning the justification of ultra-relativistic expansion velocities which do not go in line with the observed values as noted before.

Similarities between GRB 130427A and GRB 190114C, the first ever to be observed by MAGIC observatory in ultra high energy band ≥ 250 GeV, both in temporal behaviour and expected magnetic field configuration invite us to compare their light curves and modelled light curve of GRB 130427A. Since raw data from Swift satellite come from fitting the X-ray spectra based on hardness ratio rather than a concise spectral analysis as

**Figure 5.** X-ray light-curve of GRB 130427A (points with error bars) together with the optical and X-ray theoretical synchrotron light-curve (lines) from Eq. (7). We also show the electron injection power $L(t)$ given by Eq. (3).

shown on figure 5 an offset between data and model fit is expected as shown on figure 6.

As we can see taking everything else as similar, from magnetic field strength and structure to expansion velocity time dependence, there is a striking similarity of GRB 190114C and GRB 130427A which can be normalized just through scaling of the injection power from equation 3 by an factor of 0.2.

3.2. Inferring the ν NS and the binary parameters from the afterglow

Ruffini et al. (2018a) and Wang et al. (2019b) have explained the bolometric luminosity of the late afterglow by the energy release per unit time of the ν NS due to its spindown, i.e. by the ν NS rotational energy loss. For this scope we have to compute the ν NS properties, specifically radius, rotation period (or angular velocity) and magnetic field intensity and structure.

Let us first estimate the rotation period. We assume that the binary is tidally locked, i.e. the rotation period of the binary components is synchronized with the orbital period. This implies that the rotation period of the CO_{core} is $P_{\text{CO}} = P$, where P denotes the orbital period. From the Kepler law the value of P is connected to the orbital separation a_{orb} and with the binary mass as:

$$P_{\text{CO}} = P = 2\pi \sqrt{\frac{a_{\text{orb}}^3}{GM_{\text{tot}}}}, \quad (9)$$

where G is the gravitational constant and $M_{\text{tot}} = M_{\text{CO}} + M_{\text{NS}}$ is the total mass of the binary, where M_{CO} and M_{NS} are the masses of the CO_{core} and the NS companion.

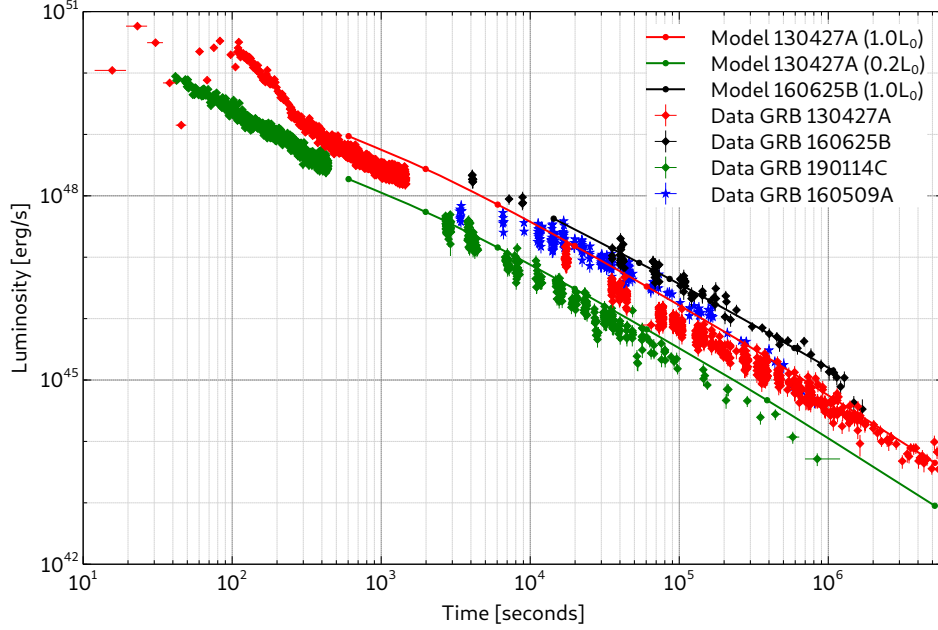


Figure 6. X-ray light-curve of GRB 160625B, GRB 130427A, GRB 190114C and GRB 160509A (black, red and green diamonds and blue stars with error bars respectively) compared with the model based light curve in Swift’s X-ray band of GRB 160625B (black line) and GRB 130427A (red line) together with the scaled down (by a factor of 0.2) fitting of GRB 130427A compared data of GRB 190114C (green line).

ion, respectively. Thus, $M_{\text{CO}} = M_{\text{Fe}} + M_{\text{ej}}$ with M_{Fe} and M_{ej} the masses of the iron core (which collapses and forms the νNS) and the ejected mass in the SN event, respectively.

The mass of the νNS is $M_{\nu\text{NS}} \approx M_{\text{Fe}}$. The rotation period, $P_{\nu\text{NS}}$, is estimated from the one of the iron core, P_{Fe} , by applying the angular momentum conservation in the collapse process, i.e.:

$$P_{\nu\text{NS}} = \left(\frac{R_{\nu\text{NS}}}{R_{\text{Fe}}} \right)^2 P, \quad (10)$$

where $R_{\nu\text{NS}}$ and R_{Fe} are the radius of the νNS and of the iron core, respectively, and we have assumed that the pre-SN star has uniform rotation; so $P_{\text{Fe}} = P_{\text{CO}} = P$.

Without loss of generality, in our estimates we can adopt a νNS order-of-magnitude radius of 10^6 cm. As we shall see below, a more careful estimate is the one of the CO_{core} progenitor (which tell us the radius of the iron core) and the orbital period/binary separation which affect additional observables of a BdHN.

It is instructive to appreciate the above statement with specific examples; for which we use the results of Wang et al. (2019b) for two BdHN archetypes: GRB 130427A for BdHN I and GRB 180827A for BdHN II. Table 3 shows, for the above GRBs, as well as for GRB 190114C, GRB 160625B and GRB 160509A, some observational quantities (the isotropic energy released E_{iso} and the cosmological redshift), the inferred BdHN type

and the properties of the νNS (rotation period $P_{\nu\text{NS}}$, rotational energy and the strength of the dipole and quadrupole magnetic field components).

By examining the BdHN models simulated in Becerra et al. (2019) (see e.g. Table 2 there), we have shown in Wang et al. (2019b) that the Model ‘25m1p08e’ fits the observational requirements of GRB 130427A, and the Model ‘25m3p1e’ the ones of GRB 180827A. These models have the same binary progenitor components: the $\approx 6.8 M_{\odot}$ CO_{core} ($R_{\text{Fe}} \sim 2 \times 10^8$ cm) developed by a $25 M_{\odot}$ ZAMS star (see Table 1 in Becerra et al. 2019) and a $2 M_{\odot}$ NS companion. For GRB 130427A the orbital period is $P = 4.8$ min (binary separation $a_{\text{orb}} \approx 1.3 \times 10^{10}$ cm), resulting in $P_{\nu\text{NS}} \approx 1.0$ ms while, for GRB 180827A, the orbital period is $P = 11.8$ min ($a_{\text{orb}} \approx 2.6 \times 10^{10}$ cm) so a less compact binary, which leads to $P_{\nu\text{NS}} \approx 2.5$ ms.

The above estimates imply that the νNS is rapidly rotating and as such it contains abundant rotational energy:

$$E = \frac{1}{2} I \Omega^2, \quad (11)$$

where I is the moment of inertia, and $\Omega = 2\pi/P_{\nu\text{NS}}$ is the angular velocity. For a millisecond NS and $I \sim 10^{45}$ g cm², the total rotational energy $E \sim 2 \times 10^{52}$ erg. Assuming that the rotational energy loss is driven by

Table 3. Observational properties of the GRB and inferred physical quantities of the ν NS of the corresponding BdHN model that fits the GRB data. Column 1: GRB name; column 2: identified BdHN type; column 3: the isotropic energy released (E_{iso}) in gamma-rays; column 4: cosmological redshift (z); column 5: ν NS rotation period ($P_{\nu\text{NS}}$), column 6: ν NS rotational energy (E_{rot}); columns 7 and 8: strength of the dipole (B_{dip}) and quadrupole (B_{quad}) magnetic field components of the ν NS. The quadrupole magnetic field component is given in a range that the upper limit is three times than the lower limit, this is brought by the freedom of inclination angles of the magnetic moment. During the fitting, we consistently assume the NS mass of $1.4M_{\odot}$ and the NS radius of 10^6 cm for all these three cases. The fitted light-curves are shown in figure 7, the parameters of GRB 1340427A and 180728A are taken from Wang et al. (2019b).

GRB	Type	Redshift	E_{iso} (erg)	$P_{\nu\text{NS}}$ (ms)	E_{rot} (erg)	B_{dip} (G)	B_{quad} (G)
130427A	BdHN I	0.34	1.40×10^{54}	0.95	3.50×10^{52}	6.0×10^{12}	$2.0 \times 10^{13} \sim 6.0 \times 10^{14}$
160509A	BdHN I	1.17	1.06×10^{54}	0.75	5.61×10^{52}	4.0×10^{12}	$1.3 \times 10^{14} \sim 4.0 \times 10^{14}$
160625B	BdHN I	1.406	3.00×10^{54}	0.5	1.26×10^{53}	1.5×10^{12}	$5.0 \times 10^{13} \sim 1.6 \times 10^{14}$
190114C	BdHN I	0.42	2.47×10^{53}	2.1	7.16×10^{51}	5.0×10^{12}	$1.5 \times 10^{15} \sim 5.0 \times 10^{15}$
180728A	BdHN II	0.117	2.73×10^{51}	3.5	2.58×10^{51}	1.0×10^{13}	$3.5 \times 10^{15} \sim 1.1 \times 10^{16}$

magnetic dipole and quadrupole radiation we have:

$$\begin{aligned} \frac{dE}{dt} &= -I\Omega\dot{\Omega} \\ &= -\frac{2}{3c^3}\Omega^4 B_{\text{dip}}^2 R_{\nu\text{NS}}^6 \sin^2 \chi_1 \left(1 + \eta^2 \frac{16}{45} \frac{R_{\nu\text{NS}}^2 \Omega^2}{c^2}\right), \end{aligned} \quad (12)$$

where

$$\eta^2 = (\cos^2 \chi_2 + 10 \sin^2 \chi_2) \frac{B_{\text{quad}}^2}{B_{\text{dip}}^2}, \quad (13)$$

with χ_1 and χ_2 the inclination angles of the magnetic moment, B_{dip} and B_{quad} are the dipole and quadrupole magnetic field, respectively. The parameter η measures the quadrupole to dipole strength ratio.

We attribute the spin-down energy of the ν NS to the energy injection of the late-time afterglow. By fitting the observed emission through the synchrotron model, the spin period and the magnetic field of the ν NS can be inferred. In Wang et al. (2019b), we have applied this approach on GRB 130427A and GRB 180728A, here we apply the same method on the recent GRB 190114C and other two, GRB 160509A and GRB 160625B, for comparison. As shown in figure 7, we plot the energy injection from the dipole and quadrupole emission of ν NS, the fitting results indicate 190114C leaves a ν NS of spin period 2.1 ms, with dipole magnetic field $B_{\text{dip}} = 5 \times 10^{12}$ G, and a quadrupole magnetic field $> 10^{15}$ G, the fitting parameters of all the GRBs are listed in table 3. Generally, the NS in the BdHN I system spins faster, of period $\lesssim 2$ ms, and contains more rotational energy $\gtrsim 10^{52}$ erg. We notice that GRB 160625B has the shortest initial spin period of $P = 0.5$ ms, which is exactly on the margin of the rotational period of a NS at the Keplerian sequence. For a NS of mass $1.4 M_{\odot}$ and radius 12 km, its Keplerian frequency $f_K \simeq 1900$ (Lattimer & Prakash

2004; Riahi et al. 2019), corresponding to the spin period of $P \simeq 0.5$ ms.

From Eq. (9) and (10), the orbital separation of binary system relates to the spin of ν NS, $a_{\text{orb}} \propto P_{\nu\text{NS}}^{2/3}$. Therefore, with the knowledge of the binary separation of GRB 130427A $\sim 1.35 \times 10^{10}$ cm, the spin period of ~ 1 ms, and the newly inferred spin of GRB 190114C ~ 1.2 ms, assuming these two systems have the same mass and radius of the CO_{core} and the ν NS, we obtain the orbital separation of GRB 190114C as $\sim 1.52 \times 10^{10}$ cm.

The self-consistent value obtained for the orbital period/separation give a strong support to our basic assumptions: 1) owing to the system compactness the binary components are tidally locked, and 2) angular momentum is conserved in the core-collapse SN process.

3.3. An additional self-consistency check

We turn now to perform a further self-consistency check of our picture. Namely, we make a cross-check of the estimated ν NS parameters obtained first from the early afterglow via synchrotron emission, and then from the late X-ray afterglow via the pulsar luminosity, with respect to expectations from NS theory.

Up to factors of order unity, the surface dipole B_s and the toroidal component B_t at a distance r from the surface are approximately related as (see, e.g., Goldreich & Julian 1969))

$$B_t \approx \left(\frac{2\pi R_{\nu\text{NS}}}{cP_{\nu\text{NS}}}\right)^2 \left(\frac{R_{\nu\text{NS}}}{r}\right) B_s. \quad (14)$$

Let us analyze the case of GRB 130427A. By equating Eqs. (6) and (14), and using the values of B_0 and R_0 from Table 1 obtained from the synchrotron analysis, and $P_{\nu\text{NS}} = P_0 \approx 1$ ms from the pulsar activity in the late afterglow analysis, we obtain $B_s \approx 2 \times 10^{13}$ G. This

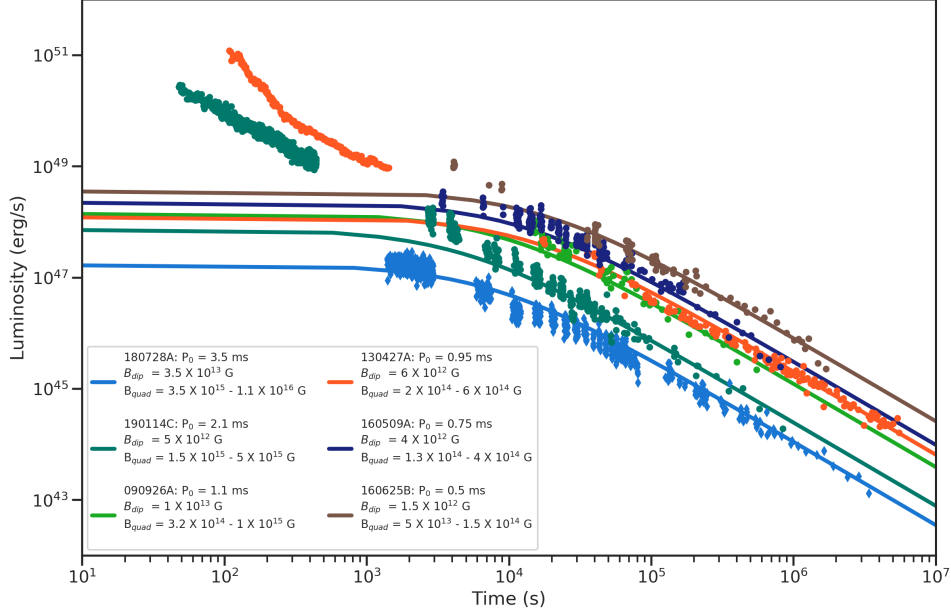


Figure 7. Afterglow powered by the ν NS pulsar: the brown, deep blue, orange, green and bright blue points correspond to the bolometric (about ~ 5 times brighter than the soft X-ray observed by Swift-XRT) light curves of GRB 160625B, 160509A, 130427A, 190114C and 180728A, respectively. The lines are the fitting of the energy injection from the rotational energy of the pulsar. The fitted parameters are shown in the legend and in table 3, the quadrupole field are given in a range, its upper value is 3 times the lower value, this is due to the oscillation angle χ_2 , which is a free parameter. The fittings of GRB 1304027A and 180728A are reproduced from Wang et al. (2019b).

value has to be compared with the one obtained from the request that the pulsar luminosity powers the late afterglow, $B_{\text{dip}} = 6 \times 10^{12}$ G (see Table 3). If we use the parameters B_0 and R_0 from Table 2 for GRB 160625B, and the corresponding $P_{\nu\text{NS}} = P_0 \approx 0.5$ ms, we obtain $B_s \approx 6.8 \times 10^{11}$ G, to be compared with $B_{\text{dip}} \approx 10^{12}$ G (see Table 3). An even better agreement can be obtained by using a more accurate value of the ν NS radius which is surely bigger than the fiducial value $R_{\nu\text{NS}} = 10^6$ cm we have used in these estimates.

4. NATURE OF THE DIPOLE+QUADRUPOLE MAGNETIC FIELD STRUCTURE OF THE ν NS

We would like to recall that it has been shown that purely poloidal field configurations are unstable against adiabatic perturbations; for non-rotating stars it has been first demonstrated by Wright (1973); Markey & Tayler (1973); see also Flowers & Ruderman (1977). For rotating stars similar results have been obtained, e.g., by Pitts & Tayler (1985). In addition, Tayler (1973) has shown that purely toroidal configurations are also unstable. We refer the reader to Spruit (1999) for a review on the different possible instabilities that may be active in magnetic stars. In this line, the dipole-quadrupole magnetic field configuration found in our analyses with a quadrupole component dominating in the early life of the ν NS are particularly relevant. They also give

support to theoretical expectations pointing to the possible stability of poloidal-toroidal magnetic field configurations on timescales longer than the collapsing time of the pre-SN star; see e.g. for details Tayler (1980); Mestel (1984).

It remains the question of how, during the process of gravitational collapse, the magnetic field increase its strength to the NS observed values. This is still one of the most relevant open questions in astrophysics which is at this stage out of the scope of the present work. We shall mention here only one important case which is the traditional explanation of the NS magnetic field strength based on the amplification of the field by magnetic flux conservation. The flux conservation implies $\Phi_i = \pi B_i R_i^2 = \Phi_f = \pi B_f R_f^2$, where i and f stand for initial and final configurations and $R_{i,f}$ the corresponding radii. The radius of the collapsing iron core is of the order of 10^8 – 10^9 cm while the radius of the ν NS is of the order of 10^6 cm; therefore, the magnetic flux conservation implies an amplification of 10^4 – 10^6 times the initial field during the ν NS formation. Therefore, a seed magnetic field of 10^7 – 10^9 G is necessary to be present in the iron core of the pre-SN star to explain a ν NS magnetic field of 10^{13} G. The highest magnetic fields observed in main-sequence stars leading to the pre-SN stars of interest are of the order of 10^4 G (Spruit 2009). If the magnetic field is uniform inside the star, then the value

of the magnetic field observed in these stars poses a serious issue to the magnetic flux conservation hypothesis for the NS magnetic field genesis. A summary of the theoretical efforts to understand the possible sources of the magnetic field of a NS can be found in [Spruit \(2009\)](#).

5. MAGNETIC FIELD AROUND THE BH AND THE HIGH-ENERGY EMISSION: THE *INNER ENGINE*

Recently, we have directed our attention to the analysis of the physical processes that can originate the observed GeV emission in energetic long GRBs (BdHN I) and the explanation of its properties, such as its precise power-law luminosity, within the BdHN picture (see [Ruffini et al. 2018f,c, 2019c](#), for details). We have used as a prototype for this study GRB 130427A ([Ruffini et al. 2018c](#)) and more recently GRB 190114C ([Ruffini et al. 2019c](#)) with its excellent observational data.

We have addressed one of the fundamental issues in relativistic astrophysics, namely how to extract the rotational energy from a Kerr BH for powering the proton synchrotron mechanism which explains the GeV emission. Our analysis of the GeV emission properties of GRB 130427A (a BdHN I) has led to the identification as “inner engine” for this BdHN I a Kerr BH of initial mass $M = 2.285M_\odot$ and angular momentum per-unit-mass $a = J/M = 0.303M$, where J is the BH angular momentum, in presence of a background uniform magnetic field of 10^{14} G aligned (but antiparallel) to the BH spin. This solution of the Einstein equations describing this kind of system has been mathematically derived by [Wald \(1974\)](#).

The rotating BH in presence of the magnetic field induces an electric field E_+ near the BH horizon ([Ruffini et al. 2018f,c](#))

$$E_+ \approx \frac{B_0 J}{2M^2}. \quad (15)$$

In [Ruffini et al. \(2018f\)](#) we have analyzed the initial *impulsive* emission process which we assumed occurs when the field E has the critical value for vacuum polarization, i.e. $E_+ = E_c$ where

$$E_c = \frac{m_e^2 c^3}{e\hbar} \quad (16)$$

with m_e and e the electron mass and charge, respectively.

The energy extraction process continues in a sequence of impulsive processes in the regime of under-critical electric field, $E_+ < E_c$. In the first process the electric potential difference $\Delta\phi$ can accelerate each proton up to $\epsilon_p = e\Delta\phi \approx 10^{21}$ eV. The total energy available in the single process, $\mathcal{E} = (1/2)E_+^2 r_+^3 \approx 10^{44}$ erg,

accelerates $N_p = \mathcal{E}/\epsilon_p \approx 10^{34}$ protons in a theoretically derived time scale of

$$\tau_{\text{th}} = \frac{\Delta\phi}{cE} = \frac{r_+}{c} \approx 10^{-6} \text{ s}, \quad (17)$$

where $r_+ = M + \sqrt{M^2 - a^2}$ is the outer BH horizon, leading to a GeV luminosity consistent with the observation ([Ruffini et al. 2018f](#)).

In a further work ([Ruffini et al. 2018c](#)) we have explicitly shown how the ultrarelativistic protons at 10^{21} eV when propagating along the polar axis, for an injection angle $\theta = 0$, give origin to UHECRs while, when propagate with $\theta \neq 0$ give origin to synchrotron emission in the GeV, TeV and PeV energies. The acceleration time of the elementary process has been theoretically computed to be:

$$\tau_{\text{th}} = 3 \times 10^{-6} \text{ s}. \quad (18)$$

We have then examined the sequence of impulsive processes which are observed with a characteristic repetition time of

$$\tau_{\text{obs}} = \frac{\mathcal{E}}{L} = 1.2 \times 10^{-6} \text{ s}, \quad (19)$$

slowly increasing with the time evolution due to the change with time of the ionic density surrounding the newborn BH (see [Ruffini et al. 2018c](#), for details). In each impulsive event we have derived the amount of decrease of the mass and spin of the BH for powering the emission and conclude that this BdHN machine can sustain the GeV emission for thousands of years.

The main conclusion is that in GRB 130427A the GeV emission observed macroscopically to be emitted continuously with a luminosity

$$L = A t^{-\alpha} \text{ erg/s} \quad (20)$$

with amplitude $A = (2.05 \pm 0.23) \times 10^{52}$ and a slope of index of $\alpha = 1.2 \pm 0.04$, in fact occurs, microscopically in a sequence of elementary impulses each lasting $\approx 10^{-6}$ seconds.

The emission of the GeV luminosity is a microscopically “discrete process” when compared and contrasted to macroscopic continuous process. It is composed of a series of $\approx 10^6$ “discrete pulses” per second, each with an energy of $\approx 10^{44}$ erg and accelerating protons to 10^{21} eV ([Ruffini et al. 2018f](#)).

6. NATURE OF THE MAGNETIC FIELD SURROUNDING THE BH

The BH in a BdHN is formed from the gravitational collapse of the NS companion. This NS follows a formation channel similar to the one of the ν NS; it is formed

from a core-collapse SN. In fact, to reach the BdHN stage the massive binary has to survive two SN events: the first SN which forms the NS and the second one which forms the ν NS (core-collapse of the CO_{core}). This can be seen from Fig. 2 that shows the evolutionary path of a massive binary leading to a BdHN I. It is then clear that the NS can have magnetic field properties similar to the ones of the ν NS, and discussed in the previous section. Therefore, the BH forms from the collapse of a magnetized NS.

The magnetic field of the collapsing NS companion should then be the responsible of the magnetic field surrounding the BH in our scenario. as we have seen, there must be a modest amplification of the initial field from the value of the NS, about 10^{13} G, to the value near the BH, about 10^{14} G. In this case, the requested amplification of the magnetic field is relatively modest and magnetic flux conservation suffices for its explanation. The BH horizon is $r_+ \sim GM/c^2$, where M can be assumed to be equal to the NS critical mass, say $3 M_{\odot}$, so $r_+ \approx 4.4$ km. The NS at the collapse point, owing to high rotation, will have a radius in excess of the typically adopted 10 km (Cipolletta et al. 2015); let's assume a conservative range 12–15 km. Under these conditions suggest magnetic flux conservation magnifies the magnetic field in the BH formation by a factor 7–12. Therefore, a seed field of 10^{13} G in the collapsing NS is enough to explain the magnetic field of 10^{14} G near the newborn BH.

It is worth to clarify a crucial point: the magnetic field has to remain anchored to some NS material which guarantee its existence. It is therefore expected that some part of the NS does not take part of the BH formation. Assuming that magnetic flux is conserved during the collapse, then the magnetic energy is a constant fraction of the gravitational energy during the entire process, so only high rotation (see, e.g., Becerra et al. 2016) and some degree of differential rotation (see, e.g., Shibata et al. 2006) of the NS at the critical mass point can be the responsible of avoiding some fraction of NS matter to remain outside with sufficient angular momentum to orbit the newborn BH.

The three-dimensional simulations of BdHNe presented in Becerra et al. (2019) show that the part of the SN ejecta surrounding the BH forms a sort of torus around it. The aforementioned matter from the NS with high angular momentum will add to this orbiting matter around the BH. In the off-equatorial directions the density is much smaller (Ruffini et al. 2018a; Becerra et al. 2019; Ruffini et al. 2019c, see also). This implies that on the equatorial plane the field is compressed while in

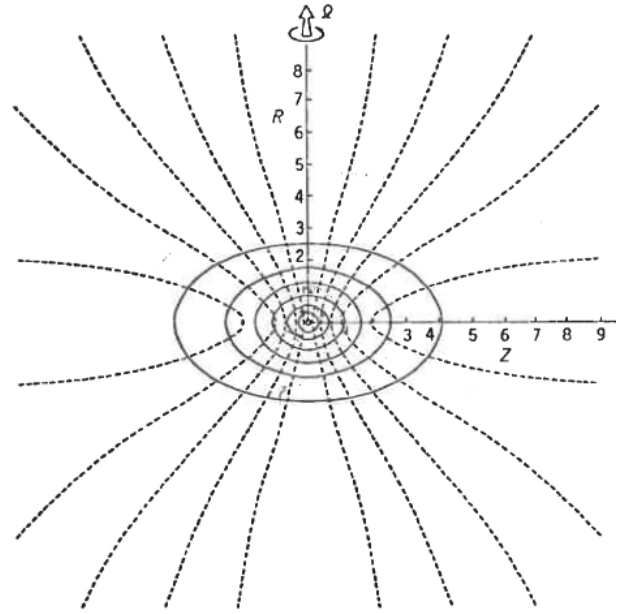


Figure 8. Figure reproduced from Wilson (1978): numerical simulation of the gravitational collapse of a star accounting for the magnetic field presence. Isodensity surfaces are indicated by the solid lines and poloidal-field lines are indicated by the dashed lines. The time is the end of the numerical simulation.

the axial direction the matter accretion flows in along the field lines.

Our *inner engine*, the BH+magnetic field configuration powering the high-energy emission in a BdHN finds additional support in numerical simulations of magnetic collapse into a BH. The first numerical, computer treatment of this process, namely the gravitational collapse to a BH in presence of magnetic fields, starts with the pioneering two-dimensional simulations by Wilson (1975) (see Fig. 8 reproduced from Wilson 1978). These works already showed the amplification of the magnetic field in the gravitational collapse process. More recent numerical simulations have indeed shown that the collapse of an unstable massive NS into a BH leads to a configuration composed of a BH surrounded by a nearly collimated magnetic field and an accretion disk (see Duez et al. 2006a; Shibata et al. 2006; Duez et al. 2006b; Stephens et al. 2007, 2008, for details). Although these simulations refer to the remnant configuration of a binary NS merger, this kind of configuration is analogous to the one developed in BdHNe, which we have applied in our recent works (see e.g. Ruffini et al. 2018a,f,c, 2019c; Wang et al. 2019b, and references therein), and which is supported by the recently presented three-dimensional simulations of BdHNe (see Becerra et al. 2019, for details).

7. CONCLUSIONS

1. We have shown how the injection of ultrarelativistic electrons from the ν NS into the magnetized expanding ejecta produces synchrotron radiation which can explain the X-ray afterglow emission. The magnetic field found by the expanding ejecta is consistent with being produced by the toroidal/longitudinal magnetic field component of the ν NS, as expected from the dominance of this component at distances much larger ($\sim 10^{12}$ cm) than the light cylinder radius in which this synchrotron emission occurs.
2. We have shown that the explanation of the afterglow and its power-law decaying luminosity via pulsar magnetic-braking radiation implies that the ν NS magnetic field has a complex dipole+quadrupole structure in which the quadrupole component is initially dominant. The strength of the dipole component is about 10^{12} – 10^{13} G while the one of the quadrupole can be of order 10^{15} G (see Fig. 6 and Table 3).
3. We have performed self-consistency checks of our picture. The ν NS parameters such as rotation period and magnetic field strength obtained for the explanation of the observed afterglow via the synchrotron radiation and the pulsar magnetic-braking emission are in close agreement (see Sec. 3.3).
4. Using the rotation period of the ν NS we have inferred the orbital period/separation which is

shown to be in agreement with the numerical simulations of the binary that explain the X-ray precursor and the time separation with the prompt emission (Wang et al. 2019b). We have shown that this self-consistency supports our assumptions of tidal synchronization of the binary and of angular momentum conservation during the gravitational collapse of the iron core leading to the ν NS.

5. A most important result of the above cross-checks is that the CO_{core} leading to the SN explosion and ejecta is the same in all the analyzed cases, independently on the BdHN type I and II.
6. The magnetic field along the rotational axis of the BH is rooted in the magnetosphere left by the rotating NS prior to the collapse and in this sense the BH uniqueness theorem applied to a BH in vacuum in an asymptotically flat space time is not applicable.
7. While in the equatorial plane the field is magnified by magnetic flux conservation in the axial direction the matter accretion flows in along the field lines; see Fig. 1 and Becerra et al. (2019).
8. As it has been recently shown, the action of the GeV, TeV, PeV radiation and UHECRs emitted along the direction of a magnetic field of 10^{14} G are a powerful process of carving a tunnel and guaranteeing the stability to the Wald mathematical solution by powerful outflows of mass-energy and radiation (see Ruffini et al. 2019a, for details).

REFERENCES

- Ackermann, M., Ajello, M., Asano, K., et al. 2014, *Science*, 343, 42
- Aharonian, F. A., Kelner, S. R., & Prosekin, A. Y. 2010, *PhRvD*, 82, 043002
- Alexander, K. D., Laskar, T., Berger, E., et al. 2017, *ApJ*, 848, 69
- Becerra, L., Bianco, C. L., Fryer, C. L., Rueda, J. A., & Ruffini, R. 2016, *ApJ*, 833, 107
- Becerra, L., Cipolletta, F., Fryer, C. L., Rueda, J. A., & Ruffini, R. 2015, *ApJ*, 812, 100
- Becerra, L., Ellinger, C. L., Fryer, C. L., Rueda, J. A., & Ruffini, R. 2019, *ApJ*, 871, 14
- Becerra, L., Guzzo, M. M., Rossi-Torres, F., et al. 2018, *ApJ*, 852, 120
- Cipolletta, F., Cherubini, C., Filippi, S., Rueda, J. A., & Ruffini, R. 2015, *PhRvD*, 92, 023007
- Duez, M. D., Liu, Y. T., Shapiro, S. L., Shibata, M., & Stephens, B. C. 2006a, *Physical Review Letters*, 96, 031101
- . 2006b, *PhRvD*, 73, 104015
- Flowers, E., & Ruderman, M. A. 1977, *ApJ*, 215, 302
- Fryer, C. L., Oliveira, F. G., Rueda, J. A., & Ruffini, R. 2015, *Physical Review Letters*, 115, 231102
- Fryer, C. L., Rueda, J. A., & Ruffini, R. 2014, *ApJL*, 793, L36
- Goldreich, P., & Julian, W. H. 1969, *ApJ*, 157, 869
- Kouveliotou, C., Granot, J., Racusin, J. L., et al. 2013, *ApJL*, 779, L1
- Laskar, T., Alexander, K. D., Berger, E., et al. 2016, *ApJ*, 833, 88
- Lattimer, J. M., & Prakash, M. 2004, *Science*, 304, 536

- Levan, A. J., Cenko, S. B., Perley, D. A., & Tanvir, N. R. 2013, *GCN Circ.*, 14455
- Li, L. 2018, *The Astrophysical Journal Supplement Series*, Accepted
- Li, L., Wang, Y., Shao, L., et al. 2018, *The Astrophysical Journal Supplement Series*, 234, 26
- Lü, H.-J., Lü, J., Zhong, S.-Q., et al. 2017, *ApJ*, 849, 71
- Markey, P., & Tayler, R. J. 1973, *MNRAS*, 163, 77
- Maselli, A., Melandri, A., Nava, L., et al. 2014, *Science*, 343, 48
- Melandri, A., Izzo, L., D’Avanzo, P., et al. 2019, *GRB Coordinates Network*, 23983
- Mestel, L. 1984, *Astronomische Nachrichten*, 305, 301
- Mirzoyan, R., Noda, K., Moretti, E., et al. 2019, *GRB Coordinates Network*, 23701
- Pitts, E., & Tayler, R. J. 1985, *MNRAS*, 216, 139
- Press, W. H., Teukolsky, S. A., Vetterling, W. T., & Flannery, B. P. 1992, *Numerical recipes in C. The art of scientific computing*
- Price, D. J. 2011, *SPLASH: An Interactive Visualization Tool for Smoothed Particle Hydrodynamics Simulations*, *Astrophysics Source Code Library*
- Riahi, R., Kalantari, S. Z., & Rueda, J. A. 2019, *PhRvD*, 99, 043004
- Rueda, J. A., & Ruffini, R. 2012, *ApJL*, 758, L7
- Ruffini, R., Karlica, M., Sahakyan, N., et al. 2018a, *ApJ*, 869, 101
- Ruffini, R., Melon Fuksman, J. D., & Vereshchagin, G. V. 2019a, *arXiv e-prints*
- Ruffini, R., Bianco, C. L., Enderli, M., et al. 2013, *GCN Circ.*, 14526
- Ruffini, R., Wang, Y., Enderli, M., et al. 2015, *ApJ*, 798, 10
- Ruffini, R., Rueda, J. A., Muccino, M., et al. 2016, *ApJ*, 832, 136
- Ruffini, R., Wang, Y., Aimuratov, Y., et al. 2018b, *ApJ*, 852, 53
- Ruffini, R., Moradi, R., Rueda, J. A., et al. 2018c, *arXiv e-prints*
- Ruffini, R., Rodriguez, J., Muccino, M., et al. 2018d, *ApJ*, 859, 30
- Ruffini, R., Becerra, L., Bianco, C. L., et al. 2018e, *ApJ*, 869, 151
- Ruffini, R., Rueda, J. A., Moradi, R., et al. 2018f, *arXiv e-prints*
- Ruffini, R., Moradi, R., Aimuratov, Y., et al. 2019b, *GRB Coordinates Network*, 23715
- Ruffini, R., Li, L., Moradi, R., et al. 2019c, *arXiv e-prints*
- Selsing, J., Fynbo, J. P. U., Heintz, K. E., Watson, D., & Dyrbye, N. 2019, *GRB Coordinates Network*, 23695
- Shibata, M., Duez, M. D., Liu, Y. T., Shapiro, S. L., & Stephens, B. C. 2006, *Physical Review Letters*, 96, 031102
- Spruit, H. C. 1999, *A&A*, 349, 189
- Spruit, H. C. 2009, in *IAU Symposium*, Vol. 259, *Cosmic Magnetic Fields: From Planets, to Stars and Galaxies*, ed. K. G. Strassmeier, A. G. Kosovichev, & J. E. Beckman, 61–74
- Stephens, B. C., Duez, M. D., Liu, Y. T., Shapiro, S. L., & Shibata, M. 2007, *Classical and Quantum Gravity*, 24, S207
- Stephens, B. C., Shapiro, S. L., & Liu, Y. T. 2008, *PhRvD*, 77, 044001
- Tam, P.-H. T., He, X.-B., Tang, Q.-W., & Wang, X.-Y. 2017, *ApJL*, 844, L7
- Tanvir, N. R., Levan, A. J., Cenko, S. B., et al. 2016, *GRB Coordinates Network*, Circular Service, No. 19419, #1 (2016), 19419
- Tayler, R. J. 1973, *MNRAS*, 161, 365
- . 1980, *MNRAS*, 191, 151
- Wald, R. M. 1974, *PhRvD*, 10, 1680
- Wald, R. M. 1974, *Phys. Rev.*, D10, 1680
- Wang, Y., Li, L., Moradi, R., & Ruffini, R. 2019a, *arXiv e-prints*
- Wang, Y., Rueda, J. A., Ruffini, R., et al. 2019b, *ApJ*, 874, 39
- Wilson, J. R. 1975, in *Annals of the New York Academy of Sciences*, Vol. 262, *Seventh Texas Symposium on Relativistic Astrophysics*, ed. P. G. Bergman, E. J. Fenyves, & L. Motz, 123–132
- Wilson, J. R. 1978, in *Physics and Astrophysics of Neutron Stars and Black Holes*, ed. R. Giacconi & R. Ruffini, 644–675
- Woosley, S. E., & Bloom, J. S. 2006, *ARA&A*, 44, 507
- Wright, G. A. E. 1973, *MNRAS*, 162, 339
- Xu, D., Malesani, D., Fynbo, J. P. U., et al. 2016, *GRB Coordinates Network*, Circular Service, No. 19600, #1 (2016), 19600
- Xu, D., de Ugarte Postigo, A., Leloudas, G., et al. 2013, *ApJ*, 776, 98
- Zhang, B.-B., Zhang, B., Castro-Tirado, A. J., et al. 2018, *Nature Astronomy*, 2, 69